

A bimodal burst energy distribution of a repeating fast radio burst source

<https://doi.org/10.1038/s41586-021-03878-5>

Received: 15 October 2020

Accepted: 5 August 2021

Published online: 13 October 2021

 Check for updates

D. Li^{1,2,17}✉, P. Wang^{1,17}, W. W. Zhu^{1,17}, B. Zhang³✉, X. X. Zhang¹, R. Duan¹, Y. K. Zhang^{1,2}, Y. Feng^{1,2,4}, N. Y. Tang^{1,5}, S. Chatterjee⁶, J. M. Cordes⁶, M. Cruces⁷, S. Dai^{1,4,8}, V. Gajjar⁹, G. Hobbs⁴, C. Jin¹, M. Kramer⁷, D. R. Lorimer^{10,11}, C. C. Miao^{1,2}, C. H. Niu¹, J. R. Niu^{1,2}, Z. C. Pan¹, L. Qian¹, L. Spitler⁷, D. Werthimer⁹, G. Q. Zhang¹², F. Y. Wang^{12,13}, X. Y. Xie¹⁴, Y. L. Yue¹, L. Zhang^{1,15}, Q. J. Zhi^{14,16} & Y. Zhu¹

The event rate, energy distribution and time-domain behaviour of repeating fast radio bursts (FRBs) contain essential information regarding their physical nature and central engine, which are as yet unknown^{1,2}. As the first precisely localized source, FRB 121102 (refs. 3–5) has been extensively observed and shows non-Poisson clustering of bursts over time and a power-law energy distribution^{6–8}. However, the extent of the energy distribution towards the fainter end was not known. Here we report the detection of 1,652 independent bursts with a peak burst rate of 122 h⁻¹, in 59.5 hours spanning 47 days. A peak in the isotropic equivalent energy distribution is found to be approximately 4.8×10^{37} erg at 1.25 GHz, below which the detection of bursts is suppressed. The burst energy distribution is bimodal, and well characterized by a combination of a log-normal function and a generalized Cauchy function. The large number of bursts in hour-long spans allows sensitive periodicity searches between 1 ms and 1,000 s. The non-detection of any periodicity or quasi-periodicity poses challenges for models involving a single rotating compact object. The high burst rate also implies that FRBs must be generated with a high radiative efficiency, disfavoured emission mechanisms with large energy requirements or contrived triggering conditions.

A continuous monitoring campaign of FRB 121102 with the Five-hundred-meter Aperture Spherical radio Telescope (FAST⁹) has been carried out since August 2019. Between 29 August and 29 October 2019, we detected 1,652 independent burst events (Supplementary Table 1) in a total of 59.5 h, covering 1.05 GHz to 1.45 GHz with 98.304- μ s sampling and 0.122-MHz frequency resolution. The total number of previously published bursts from this source was 347 (refs. 7,8 and <http://www.frbcatalog.org>). The flux limit of this burst sample is at least three times lower than those of previous observations. The cadence and depth of the observations allow for a statistical study of the repeating bursts, revealing several previously unseen characteristics. The burst statistics are shown as a function of time (Fig. 1), with the accumulated counts in 1-h bins in Fig. 1a and the day-to-day average burst rates in Fig. 1b. The burst rate peaked at 122 h⁻¹ on 7 September and at 117 h⁻¹ on 1 October, both measured over the respective averaged 1-h sessions. In both instances, the burst rate dropped precipitously afterwards. Burst energies are plotted against epoch (Fig. 1c), and together with the energy histogram (Fig. 1d), demonstrate bimodality that is itself a function of epoch.

We measured the peak flux density, pulse width and fluence for each burst. Given the redshift $z = 0.193$ (ref. 5), we adopted the corresponding luminosity distance $D_L = 949$ Mpc based on the latest cosmological parameters measured by the Planck team¹⁰ and calculated the isotropic equivalent energy of each burst at 1.25 GHz (Methods). The derived energies span more than three orders of magnitude, from below 10^{37} erg to near 10^{40} erg. Figure 2 presents the histogram of the bursts (bottom panel) and the cumulative counts as a function of energy (top panel). With a prominent peak and two broad bumps, the distribution cannot be fit by a single power law or a single log-normal function (Table 1). A satisfactory fit can be achieved with a log-normal distribution plus a generalized Cauchy function:

$$N(E) = \frac{N_0}{\sqrt{2\pi}\sigma_E E} \exp\left[-\frac{(\log E - \log E_0)^2}{2\sigma_E^2}\right] + \frac{\epsilon_E}{1 + (E/E_0)^{\alpha_E}}, \quad (1)$$

where $\epsilon_E = 0$ for $E < 10^{38}$ erg and $\epsilon_E = 1$ for $E > 10^{38}$ erg. The characteristic energy E_0 is 4.8×10^{37} erg and is robust against uncertainties in detection threshold and choices of pipelines (Methods). The best-fit distribution

¹CAS Key Laboratory of FAST, NAOC, Chinese Academy of Sciences, Beijing, China. ²University of Chinese Academy of Sciences, Beijing, China. ³Department of Physics and Astronomy, University of Nevada, Las Vegas, Las Vegas, NV, USA. ⁴CSIRO Astronomy and Space Science, Epping, New South Wales, Australia. ⁵Department of Physics, Anhui Normal University, Wuhu, China. ⁶Cornell Center for Astrophysics and Planetary Science and Department of Astronomy, Cornell University, Ithaca, NY, USA. ⁷Max-Planck-Institut für Radioastronomie, Bonn, Germany. ⁸Western Sydney University, Penrith, New South Wales, Australia. ⁹Department of Astronomy, University of California Berkeley, Berkeley, CA, USA. ¹⁰Department of Physics and Astronomy, West Virginia University, Morgantown, WV, USA. ¹¹Center for Gravitational Waves and Cosmology, West Virginia University, Morgantown, WV, USA. ¹²School of Astronomy and Space Science, Nanjing University, Nanjing, China. ¹³Key Laboratory of Modern Astronomy and Astrophysics (Nanjing University), Ministry of Education, Nanjing, China. ¹⁴Guizhou Normal University, Guiyang, China. ¹⁵School of Physics and Technology, Wuhan University, Wuhan, China. ¹⁶Guizhou Provincial Key Laboratory of Radio Astronomy and Data Processing, Guizhou Normal University, Guiyang, China. ¹⁷These authors contributed equally: D. Li, P. Wang, W. W. Zhu. ✉e-mail: dili@nao.cas.cn; zhang@physics.unlv.edu

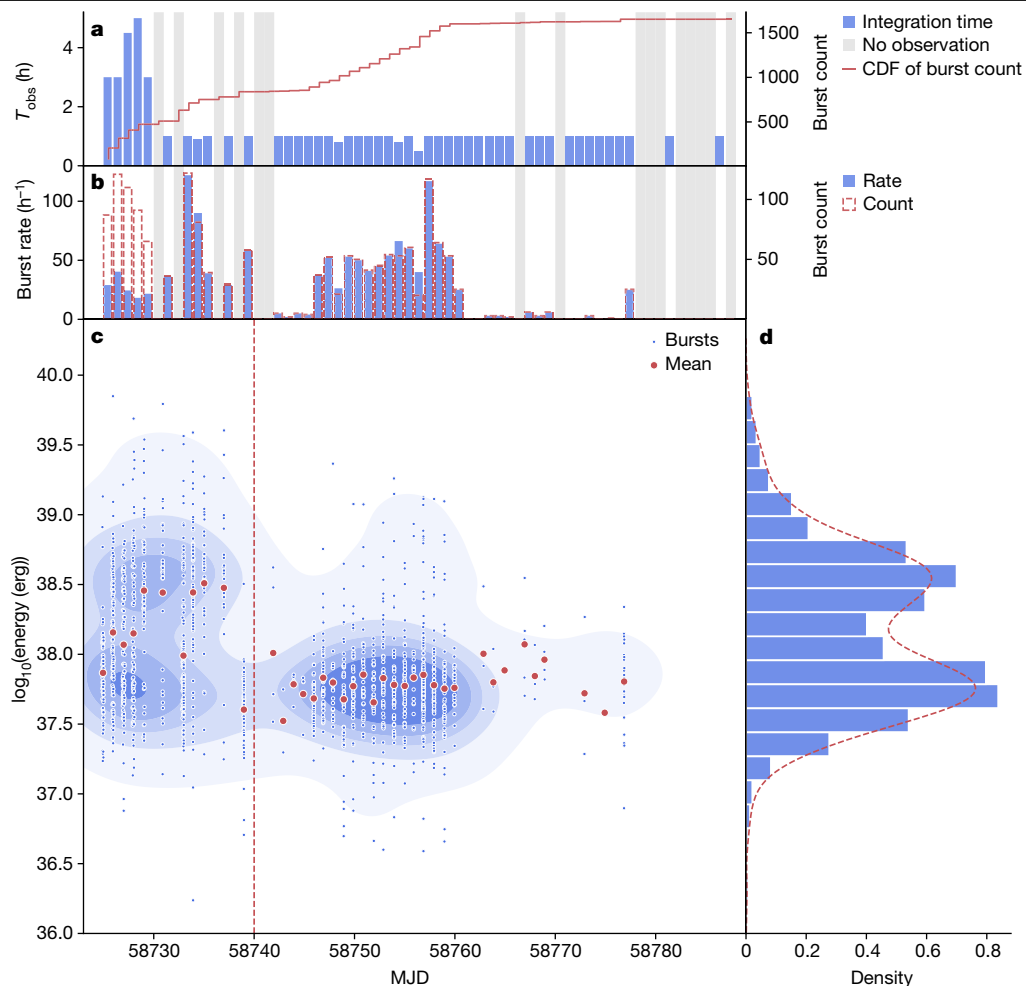


Fig. 1 | Detected bursts and temporal energy distribution during the observation campaign. **a**, The duration of each observation session (blue bar) and the cumulative number distribution of the bursts (red solid line). **b**, The rate (blue bar) and count (red dashed line) of the bursts detected. The grey shaded bars show days without observations. **c**, Time-dependent burst energy

distribution. The blue dots are all of the 1,652 bursts, the red dots represent the average value for each observation session. The blue contour is the 2D kernel density estimation (KDE) of the bursts. **d**, The isotropic energy histogram of the bursts detected before MJD 58740 (14 September 2019); the red dashed line represents the KDE of this distribution.

index is $\alpha_E = 1.85 \pm 0.30$. At high energies, a simple power law consistent with the results derived from previous bursts^{8,11} can describe the distribution reasonably well. It is clear that no single functional form can fit the data in the full energy range. At the low energy end, the log-normal distribution is consistent with a stochastic process. At the high-energy end, the generalized Cauchy function describes a steepening power law with an asymptotic slope of α_E . Mathematically, a Cauchy distribution, also known as a Cauchy–Lorentz distribution, also describes the ratio of two independent, normally distributed random variables. The bimodality of the energy distribution is also time-dependent—the high-energy mode has more events before modified Julian date (MJD) 58740—which also helps to rule out that the bimodality is an artefact due to significant drifts in system calibration over time.

Each pulse time of arrival was transformed to the solar system barycentre using the DE405 ephemeris. No periodicity between 1 ms to 1,000 s could be found in the power spectrum calculated using either the phase-folding or the Lomb–Scargle periodogram (Methods).

The waiting time between two adjacent (detected) bursts is $\delta t = t_{i+1} - t_i$, where t_{i+1} and t_i are the arrival times for the $(i + 1)$ th and (i) th bursts, respectively. All waiting times were calculated for pulses within the same session to avoid long gaps of about 24 h. The distribution of the waiting times (Fig. 3) has a dominant feature that can be well fit by a log-normal function centred at 70 ± 12 s. Selecting only high-energy pulses $E > 3 \times 10^{38}$ erg, the peak moves to 220 s. The waiting time distribution

and absence of periodicity are generally consistent with previous findings for FRB 121102 (refs. ^{7,8,12,13}) and can be reproduced within the uncertainties by simulating bursts arriving randomly in time. For example, the location of the peak of the log-normal distribution can be obtained with a Monte Carlo simulation mimicking the sampling cadence and number of detections of the real observations (Methods). The peaks around 70 s and 220 s in the waiting time distribution are close to the average values for the respective samples (full and high energy). This is consistent with the waiting time distribution being a combination of a stochastic process and the lack of sampling for time scales longer than about 1,000 s. The secondary peak centred at approximately 3.4 ms, however, is most probably due to substructure of individual bursts, although some may be closely spaced, independent bursts.

The waiting time distribution and absence of a periodicity are in sharp contrast to expectations from standard radio pulsars, which involve stable rotation and emission in narrow beams from a narrow range of altitudes. If FRB 121102 involves a rotating object, the periodicity can be erased if beam directions and altitudes are sufficiently stochastic, introducing scatter in arrival times and reducing any features in the power spectrum or waiting time distribution that would signify periodicity. Nevertheless, the 70-s waiting-time peak still places an upper bound on the underlying period.

The optimal dispersion measure (DM) of the bursts is constrained to 565.8 ± 0.9 pc cm⁻³ between MJD 58724 and MJD 58776 (Methods). This

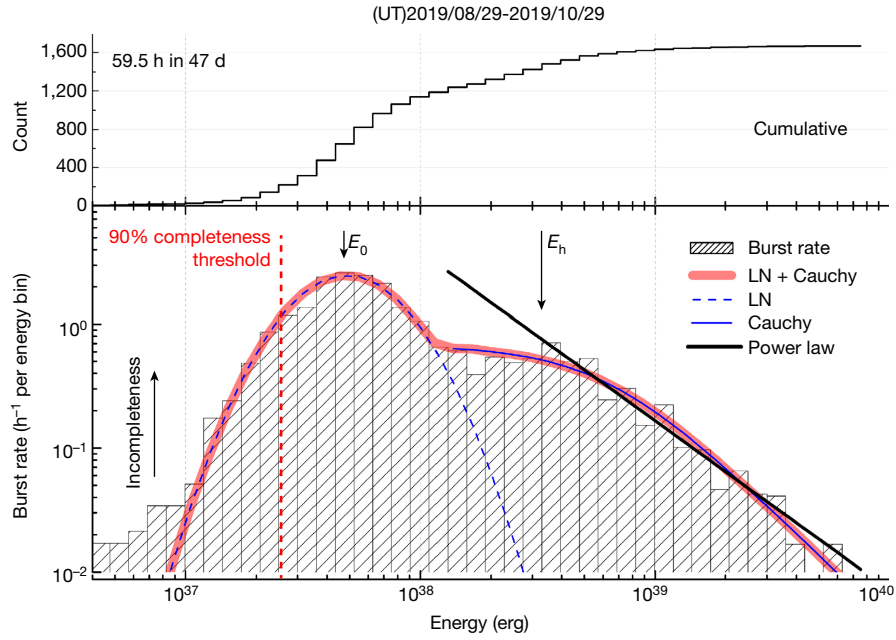


Fig. 2 | Burst rate distribution of the isotropic equivalent energy at 1.25 GHz for FRB 121102 bursts. The bimodal ‘lognormal (LN) (dashed blue) + Cauchy (solid blue)’ distribution is shown in red and a single power-law fit for bursts above a certain threshold $E \geq E_h = 3 \times 10^{38}$ erg is shown in black. The 90% detection completeness threshold is shown by the red dashed line,

suggests that the DM of FRB 121102 has increased by about 5–8 pc cm⁻³ (or about 1.0–1.4%) compared to earlier detections^{14–16}, confirming a trend seen before¹⁷ but this time with a larger significance level (Fig. 4). Combining all of the data, the average slope is

$$\frac{dDM}{dt} = +0.85 \pm 0.10 \text{ pc cm}^{-3} \text{ yr}^{-1}. \quad (2)$$

The long-term trend relies heavily on earlier measurements, which is further explored in the Methods. This is inconsistent with the

Table 1 | The fitted parameters of the isotropic equivalent energy distribution

Function	Fitting parameter	Energy range (erg)	R ^{2a}
Power law	$\gamma = -0.61 \pm 0.04$	$4 \times 10^{36} \leq E \leq 8 \times 10^{39}$	0.104(6) ^b
	$\gamma = -1.37 \pm 0.18$	$3 \times 10^{38} \leq E \leq 8 \times 10^{39}$	0.999(1)
log-normal	$E_0 = 7.62 \times 10^{37}$ (erg)		
	$N_0 = 2.20 \times 10^{38}$	$4 \times 10^{36} \leq E \leq 8 \times 10^{39}$	0.85(8)
	$\sigma_E = 0.54$		
Cauchy	$E_0 = 8.16 \times 10^{38}$ (erg)	$4 \times 10^{36} \leq E \leq 8 \times 10^{39}$	0.075(1)
	$\alpha_E = 3.02 \pm 0.5$		
log-normal + Cauchy	$E_0 = 7.2 \times 10^{37}$ (erg)		
	$N_0 = 2.06 \times 10^{38}$	$4 \times 10^{36} \leq E \leq 8 \times 10^{39}$	0.925(8)
	$\sigma_E = 0.52$		
	$\alpha_E = 1.85 \pm 0.3$		

^aCoefficient of determination. $R^2 = 1 - S(\text{res}/S_{\text{tot}}) * [(n-1)/(n-p-1)]$, where S_{tot} is the total sum of squares from data and S_{res} is the minimum fitting residual sum of squares.

^bUncertainties in parentheses refer to the last quoted digit.

corresponding to $E_{90} = 2.5 \times 10^{37}$ erg for an assumed pulse width of 3 ms and scaling as the square root of the pulse width (Extended Data Fig. 6). The missed weak bursts below E_{90} , as indicated by the upward arrow, will make the log-normal distribution wider, but will not affect the location of the peak E_0 (Methods).

decreasing trend predicted for a freely expanding shell (for example, a supernova remnant) around the FRB source¹⁸, but is consistent with such a shell during the deceleration (Sedov–Taylor) phase¹⁹.

We detected no polarization in the bursts at 1.4 GHz, in contrast with higher frequency observations⁶ but consistent with previous results at similar frequencies¹⁷ (Methods).

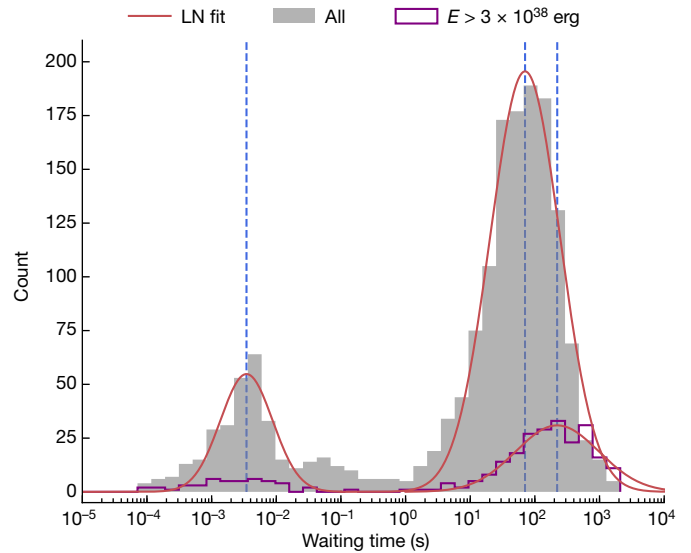


Fig. 3 | Waiting time distribution of the bursts. The grey bar and solid red curve show the distribution of waiting time and its log-normal (LN) fit. The high-energy component ($E > 3 \times 10^{38}$ erg) is shown by a solid purple line. The three fitted peak waiting times (blue dashed vertical lines) from left to right are 3.4 ± 1.0 ms, 70 ± 12 s, and 220 ± 100 s. The peaks around 70 s and 220 s in the waiting time distribution are close to the average values for the respective samples (full and high energy). This is consistent with a stochastic process (see the main text and Methods for further discussion).

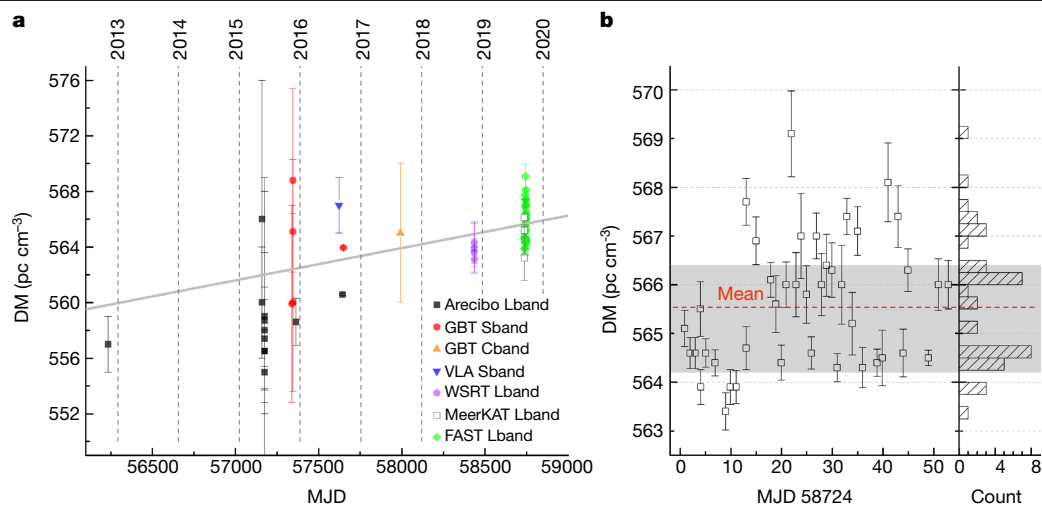


Fig. 4 | DM evolution of FRB 121102. a, Temporal DM variation for FRB 121102 over a 9-year period. The solid grey line denotes the linear fit with slope $+0.85 \pm 0.10 \text{ pc cm}^{-3} \text{ yr}^{-1}$. **b**, The distribution of DM estimates for the brightest

burst on each day of FAST observations. The red dashed line indicates the average DM of 565.6 pc cm^{-3} during the FAST observations, and the grey region shows the 95% confidence level.

The large sample of bursts sheds new light on theoretical models of FRBs. The isotropic equivalent energy distribution (or energy function) necessitates a bimodal fit, suggesting possibly more than one emission mechanism or emission site or beam shape. The log-normal distribution characterizes the weaker bursts, the generation of which may become less efficient below the characteristic energy scale of $E_0 \sim 4.8 \times 10^{37}$ ergs. Some magnetar models do predict a luminosity lower bound for producing FRBs^{20,21}, and the reported E_0 value may be interpreted by adjusting parameters within these models.

As shown in Fig. 3, the distribution of the time intervals between bursts (henceforth referred to as the waiting times) is log-normal in form. This behaviour is similar to that observed in other astrophysical bursting events such as soft gamma-ray repeaters^{22–26}. The extremely high burst rate revealed by our observational campaign poses challenges to some models invoking emission^{20,21} or persistent magnetosphere interactions²⁷ are attractive options but require masking of the rotational periodicity by stochastic beaming, by large variations in emission altitude, or by propagation delays.

The frequent triggers of bursts also constrain coherent radiation models. In particular, the popular synchrotron maser models demand well-ordered magnetic field lines in the upstream regions of the shock^{28,29}. Clustered FRBs require successive shocks propagating into the previously shocked medium, which is hot and probably with distorted magnetic field lines. The short waiting times therefore challenge these models regarding whether coherent emission can be emitted with such short waiting times.

The synchrotron maser mechanism is also very inefficient^{28,29}. The total isotropic energy emitted in the 1,652 bursts that we report is 3.4×10^{41} erg. Adopting a typical radiative efficiency, the total isotropic energy output during our 47-day observational campaign is already about 37.6% of the available magnetar energy. The estimation would not change significantly even considering beaming effect (Methods). Conversely, coherent emission mechanisms that invoke a neutron star magnetosphere^{20,30} can radiate in the radio band much more efficiently, and are therefore preferred by the data.

Online content

Any methods, additional references, Nature Research reporting summaries, source data, extended data, supplementary information,

acknowledgements, peer review information; details of author contributions and competing interests; and statements of data and code availability are available at <https://doi.org/10.1038/s41586-021-03878-5>.

- Petroff, E., Hessels, J. W. T. & Lorimer, D. R. Fast radio bursts. *Astron. Astrophys. Rev.* **27**, 4 (2019).
- Cordes, J. M. & Chatterjee, S. Fast radio bursts: an extragalactic enigma. *Ann. Rev. Astron. Astrophys.* **57**, 417–465 (2019).
- Spitler, L. G. et al. A repeating fast radio burst. *Nature* **531**, 202–205 (2016).
- Chatterjee, S. et al. A direct localization of a fast radio burst and its host. *Nature* **541**, 58–61 (2017).
- Tendulkar, S. P. et al. The host galaxy and redshift of the repeating fast radio burst FRB 121102. *Astrophys. J. Lett.* **834**, L7 (2017).
- Michilli, D. et al. An extrememagneto-ionic environment associated with the fast radio burst source FRB 121102. *Nature* **553**, 182 (2018).
- Zhang, Y. G. et al. Fast radio burst 121102 pulse detection and periodicity: a machine learning approach. *Astrophys. J.* **866**, 149 (2018).
- Gourdji, K. et al. A sample of low-energy bursts from FRB 121102. *Astrophys. J. Lett.* **877**, L19 (2019).
- Li, Di. et al. FAST in space: considerations for a multibeam, multipurpose survey using China's 500-m aperture spherical radio telescope (FAST). *IEEE* **19**, 112–119 (2018).
- Planck Collaboration et al. Planck 2015 results. XIII. Cosmological parameters. *Astron. Astrophys.* **594**, A13 (2016).
- Shannon, R. M. et al. The dispersion-brightness relation for fast radio bursts from a wide-field survey. *Nature* **562**, 386–390 (2018).
- Katz, J. I. Fast radio bursts. *Prog. Part. Nucl. Phys.* **103**, 1–18 (2018).
- Palaniswamy, D., Li, Y. & Zhang, B. Are there multiple populations of fast radio bursts? *Astrophys. J. Lett.* **854**, L12 (2018).
- Scholz, P. et al. The repeating fast radio burst FRB 121102: multi-wavelength observations and additional bursts. *Astrophys. J.* **833**, 177 (2016).
- Petroff, E. et al. FRBCAT: the fast radio burst catalogue. *Publ. Astron. Soc. Aust.* **33**, e045 (2016).
- Oostrum, L. C. et al. Repeating fast radio bursts with WSRT/Apertif. *Astron. Astrophys.* **635**, A61 (2020).
- Hessels, J. W. T. et al. FRB 121102 bursts show complex time-frequency structure. *Astrophys. J.* **876**, L23 (2019).
- Metzger, B. D., Berger, E. & Margalit, B. Millisecond magnetar birth connects FRB 121102 to superluminous supernovae and long-duration gamma-ray bursts. *Astrophys. J.* **841**, 14 (2017).
- Yang, Y.-P. & Zhang, B. Dispersion measure variation of repeating fast radio burst sources. *Astrophys. J.* **847**, 22 (2017).
- Lu, W. B., Kumar, P. & Zhang, B. A unified picture of Galactic and cosmological fast radio bursts. *Mon. Not. R. Astron. Soc.* **498**, 1397 (2020).
- Wadiasingh, Z. et al. The fast radio burst luminosity function and death line in the low twist magnetar model. *Astrophys. J.* **891**, 82 (2020).
- Göğüş, E. et al. Statistical properties of SGR 1806-20 bursts. *Astrophys. J. Lett.* **532**, L121–L124 (2000).
- Wang, F. Y. & Yu, H. SGR-like behaviour of the repeating FRB 121102. *JCAP* **03**, 023 (2017).
- Bagchi, M. A unified model for repeating and non-repeating fast radio bursts. *Astrophys. J. Lett.* **838**, L16 (2017).

25. Smallwood, J. L., Martin, R. G. & Zhang, B. Investigation of the asteroid-neutron star collision model for the repeating fast radio bursts. *Mon. Not. R. Astron. Soc.* **485**, 1367–1376 (2019).
26. Cordes, J. M. & Wasserman, I. Supergiant pulses from extragalactic neutron stars. *Mon. Not. R. Astron. Soc.* **457**, 232–257 (2016).
27. Zhang, B. Fast radio bursts from interacting binary neutron star systems. *Astrophys. J. Lett.* **890**, L24 (2020).
28. Metzger, B. D., Margalit, B. & Sironi, L. Fast radio bursts as synchrotron maser emission from decelerating relativistic blast waves. *Mon. Not. R. Astron. Soc.* **485**, 4091–4106 (2019).
29. Beloborodov, A. M. Blast waves from magnetar flares and fast radio bursts. Preprint at <https://arxiv.org/abs/1908.07743> (2019).
30. Kumar, P., Lu, W. & Bhattacharya, M. Fast radio burst source properties and curvature radiation model. *Mon. Not. R. Astron. Soc.* **468**, 2726–2739 (2017).

Publisher's note Springer Nature remains neutral with regard to jurisdictional claims in published maps and institutional affiliations.

© The Author(s), under exclusive licence to Springer Nature Limited 2021, corrected publication 2021

Methods

Search procedures and burst energetics

We carried out blind searches using two separate software packages, Heimdall³¹ and Presto³², with the same search parameter space ($DM = 400$ to 650 pc cm^{-3} , DM step of 0.2 pc cm^{-3} , and threshold $S_{\text{peak}}/\text{Noise} \geq 7$). Burst candidates resulting from both searches were kept for further inspections. The dynamic spectra of all candidates in both the $DM = 0$ time series and the de-dispersed time series at 565 pc cm^{-3} were generated and then manually checked to ensure that the surviving candidates have a plausible dispersion sweep and to filter out radio frequency interference (RFI) events.

To obtain high-quality flux density and polarization calibration solutions, a 1 K equivalent noise calibration signal was injected before each session, which was used to scale data to T_{sys} units. The off-pulse brightness (mK s) of the first pulse in each session is shown in Extended Data Fig. 1 (bottom). The standard deviation of off-pulse brightness is constant within 6% for all observations. The variation in the off-pulse level comes mainly from the zenith angle dependence of the telescope gain. Kelvin units were then converted to mJy using the zenith angle-dependent gain curve, provided by the observatory through quasar measurements. The zenith-angle-dependent gain applied for each pulse is shown in Extended Data Fig. 1 (top). The red dots denote the average gain in each day. For most days, the pulses that have brightness closest to the average value were taken at zenith angles < 15 degrees, which corresponds to a stable gain of 16 K Jy^{-1} .

We calculated the isotropic equivalent burst energy, E , following equation 9 in ref. ³³:

$$E = (10^{39} \text{ erg}) \frac{4\pi}{1+z} \left(\frac{D_L}{10^{28} \text{ cm}} \right)^2 \left(\frac{F_v}{\text{Jy} \cdot \text{ms}} \right) \left(\frac{\nu_c}{\text{GHz}} \right), \quad (3)$$

where $F_v = S_v \times W_{\text{eq}}$ is the specific fluence in units of $\text{erg cm}^{-2} \text{ Hz}^{-1}$ or $\text{Jy} \cdot \text{ms}$, S_v is the peak flux density that has been calibrated with the noise level of the baseline, with the amount of pulsed flux above the baseline then measured, giving the flux measurement for each pulse at a central frequency of $\nu_c = 1.25 \text{ GHz}$, W_{eq} is the equivalent burst duration, and the luminosity distance $D_L = 949 \text{ Mpc}$ corresponds to a redshift of $z = 0.193$ for FRB 121102 (ref. ⁵).

Detection threshold and completeness

The combined effect of the sometimes bandwidth-limited structure of FRB bursts and RFI events, particularly the satellite bands around 1.2 GHz, affects the actual sensitivity of detection. The representative $7\text{-}\sigma$ detection threshold in the FAST campaign is 0.015 Jy ms assuming a 1-ms-wide burst in terms of integrated flux (fluence), which is a few times more sensitive than that previously available from Arecibo.

To quantify the detection completeness, we differentiate two kinds of signal-to-noise ratios (SNR), namely, the peak flux SNR_p and the fluence flux SNR_f (corresponding to integrated flux and in turn energy). Even for the same pulses, SNR_p and SNR_f behave differently (Extended Data Figs. 3, right, 4). The complexities and the deviation from the radiometer equation mainly arise from two ‘non-Gaussian’ aspects in the detection processes. First, the detection software (for example, Heimdall or Presto) uses the pulse peak SNR_p as the initial selection criterion. Then downsampling approximate matched filtering (often just a box-car sum) in time is used to maximize the SNR_f by comparing a series of trial-smoothing results with different widths in time. The candidates are then subject to visual inspection. Second, the instrumental background is often RFI-limited (Extended Data Fig. 2), particularly when the pulse is weak and/or bandwidth-limited (where the dispersed pulse covers only a fraction of the passband); for example, a ‘weak’ (peak flux $< 7\sigma$) but more ‘complete’ pulse, with a sweep covering the full band and a larger pulse width, is more easily identified through visual inspection.

To quantify these effects, we carried out an experiment by adding simulated pulses into real data (Extended Data Fig. 3, left). All pulses were generated assuming $DM = 565 \text{ pc cm}^{-3}$ and a Gaussian pulse profile (in frequency) and then sampled in time and frequency in exactly the same fashion as for the FAST data. The frequency bandwidth of pulses is sampled from a normal distribution, similar to that of the observed pulses. The pulse width (in time) was sampled from a log-normal distribution, similar to that of the observed FRB bursts. The SNR_p of the injected pulses was defined as the peak flux divided by the measured RMS of the real data. More than 1,000 mock FRB bursts were injected into 20 min of FAST data. We then processed the simulated datasets through the same pipelines and procedures. As shown in Extended Data Fig. 3 (left), the simulated pulses with sufficient SNR_f can be distinguished from RFI and thus detected, whereas weaker ones cannot. Histograms of the peak flux SNR_p and the integrated flux SNR_f are shown in Extended Data Fig. 3 (right). The behaviours were similar to the previously published simulations³⁴.

Both detection and fluence completeness are shown in Extended Data Fig. 4, which shows the recovered fraction of injected ‘FRB’ pulses as a function of burst fluence and duration. For reference, the 90 per cent detection completeness threshold for a characteristic width of 3 ms occurs at a fluence of 0.02 Jy ms , roughly corresponding to $E_{90} = 2.5 \times 10^{37} \text{ erg}$. At a given fluence, the longer durations tend to be more incomplete. Extended Data Figure 4 shows that the search has a high detection completeness ($> 95\%$) for burst durations of $< 20 \text{ ms}$ when the burst fluence is $> 0.06 \text{ Jy ms}$, which corresponds to an energy of $> 7.5 \times 10^{37} \text{ erg}$. Below this energy, the survey will begin to miss wider bursts. The current detections are consistent with event rate starting to drop below E_0 .

We produce a ‘reconstructed’ energy distribution, by adding the missing fraction back into the sample (Extended Data Fig. 5a) based on the simulated recovery rate. The reconstructed energy distribution has a wider log-normal distribution for the low-energy pulses, but the same peak E_0 . We reaffirm the existence and robustness of the peak location in this simulation.

Energy distribution

The histogram of burst energies exhibits two clearly separable bumps, which can be well fit by two log-normal functions (Extended Data Fig. 5b, top).

The burst rate versus burst energy distribution shows a broad bump centred around $4.8 \times 10^{37} \text{ erg}$ and a power-law-like distribution with a slope close to -2 for the high-energy tail. We first fit the distribution with a single power law, Cauchy, and log-normal function, respectively. The χ^2 and R^2 tests in Table 1 show that these single-component models cannot adequately describe the data.

We then test the hypothesis that the energy distribution can be described by a power-law function $N(E) = N_1 E^{-\alpha_E}$ in certain energy range $E_i \leq E \leq E_f$. That is,

$$N_1 = \frac{N_{\text{ev}}(1 - \alpha_E)}{E_f^{1-\alpha_E} - E_i^{1-\alpha_E}}, \quad (4)$$

where N_1 is a normalization constant, and N_{ev} is the total number of bursts included. For $3 \times 10^{38} \leq E \leq 8 \times 10^{39} \text{ erg}$, the energy function is consistent with a power law with $\alpha_E = 1.85 \pm 0.3$. Previous studies also found power-law energy distributions for the Australian square kilometre array pathfinder (ASKAP) sample and all of the bursts from the FRB catalogue^{8,11,23,35-38}. A bimodal distribution is clearly needed to properly cover the full energy range. A log-normal function plus a Cauchy function for the high-energy range can achieve a satisfactory fit, with a coefficient of determination $R^2 = 0.928$.

Giant pulses from the Crab pulsar show a power-law amplitude distribution combined with a long tail of ‘supergiant pulses’³⁹ due to underlying magnetospheric physics that might help to elucidate the energy distribution of FRB 121102. However, the Crab’s giant pulses are manifestly tied to the spin of the neutron star, whereas the bursts discussed here are not

periodic. Therefore, a mechanism is needed to erase the periodicity in detected bursts; this could be caused by large variations in altitude or beaming that are not strictly tied to the rotating neutron star. It could also be caused by propagation effects in the circumsource medium.

The low-energy component is similar to distributions seen in many radio pulsars. At the high-energy end, the trend towards a power law with slope α_L is reminiscent of giant pulses from the Crab pulsar. The bimodality of the energy distribution is also clearly time dependent, with the high-energy mode having more events before MJD 58740. The fewer high-energy events after that epoch may signify that the bimodality is due to time-dependent lensing but more plausibly might be an analogue of ‘mode changes’ commonly seen in long period radio pulsars where pulse components change their relative amplitudes and occurrence rates. Further observations can distinguish between these possibilities.

In Fig. 1, temporal variations are seen for the collective behaviour of each session. There are days with significantly brighter averages, although weak bursts are always present.

Analysis with a modified Cauchy function

A common Cauchy distribution is

$$p(x) = \frac{1}{\pi(x^2 + 1)} \quad (5)$$

Cauchy distribution can also be obtained from the distribution of the ratio of two independent normally distributed random variables with zero mean.

Assume that X and Y are independent of each other and obey a normal distribution:

$$f_{X|Y(x)} = \frac{1}{\sqrt{2\pi}} e^{-x^2/2} \quad (6)$$

Then the probability density of $Z = X/Y$ is:

$$\begin{aligned} f_{X/Y}(z) &= \int_{-\infty}^{\infty} |y| f(y, yz) dy \\ &= \int_{-\infty}^{\infty} |y| f(y) f(yz) dy \\ &= \frac{1}{2\pi} \int_{-\infty}^{\infty} |y| e^{-y^2/2} e^{-y^2 z^2/2} dy \\ &= \frac{1}{\pi} \int_0^{\infty} y e^{-(z^2+1)y^2/2} dy \\ &= \frac{1}{2\pi} \int_0^{\infty} e^{-(z^2+1)u/2} du \\ &= \frac{1}{2\pi} \frac{2}{(z^2+1)} \\ &= \frac{1}{\pi(z^2+1)} \end{aligned} \quad (7)$$

Hence, if we change the index 2 of the normal distribution to alpha, then the Cauchy distribution will be the general Cauchy function:

$$p(x) = \frac{1}{\pi(x^\alpha + 1)} \quad (8)$$

The generalized Cauchy function can describe the ratio between two normally distributed variables. The best-fit index of 1.85 is close to 2 with $\sigma = 0.3$, which could suggest correlated events for generating strong bursts.

Width distribution

The pulse width W_{eq} is shown against flux density and the pulse width distribution of the bursts (Extended Data Fig. 6, left and right, respectively). The equivalent width W_{eq} is defined as the width of a rectangular burst that has the same area as the bursts, with the height of peak

flux density denoted as S_{peak} . In our sample, several pulses might be described as multiple components in a single burst, if there is ‘bridge’ emission (higher than 5σ) between pulses for the bursts with a complex time-frequency structure. This results in some bursts having overestimated equivalent widths. The computed equivalent widths range from 0.43 ms to about 40 ms, consistent with a log-normal distribution centred around approximately 4 ms. This is consistent with the known statistical properties of repeating FRBs^{40,41}.

Monte Carlo simulations of the waiting time distribution

Following the exact setup of the observations, including starting time, duration, sampling rate and pulse burst rate, we generate random times of arrival through Monte Carlo simulations. The simulation was performed three times, with numbers of generated pulses of $100 \times 1,652 = 1.6e5$, $1 \times 1,652 = 1652$ and $0.2 \times 1,652 = 330$. The distributions of different waiting time sets are shown in Extended Data Fig. 7. The log-normal distribution appears in the randomly generated waiting time distribution, and centred at 0.62 s, 61.89 s and 272.04 s.

The peak waiting time of the log-normal distribution increases as the number of bursts in the simulated sample decreases. Among the 1,652 pulses of FRB 121102, 296 have higher energy than 3×10^{38} erg, which accounts for about one-fifth of the total pulses. The peak waiting time of these 296 pulses is 220 s, which is close to the peak waiting time from the generated $0.2 \times 1,652 = 330$ pulses. The main feature of waiting is the log-normal distribution centred at 70 s, which is close to the simulated distribution with 1,652 generated pulses.

Our simulations suggest that the observed log-normal distributions of waiting time centred at 70 s and 220 s, though not an instrumental effect, are nevertheless consistent with emission from a source that emits FRBs randomly or other ‘masking’ factors, such as rotating attitudes.

Periodicity search

The Lomb–Scargle periodogram method^{42,43} is widely used to identify periodicities in data that are not uniformly sampled.

We apply this method to the times of arrival of FRB121102 to determine whether there is a possible period. If the bursts of FRB121102 do have a period, folding the burst arrival times according to this period would show clustering in burst phase.

Periodograms of bursts from FRB121102 for periods ranging from 1 ms to 100 d are shown in Extended Data Fig. 8; the left panel covers periods from 0.01 d to 100 d and the right panel periods from 1 ms to 1,000 s. Of the five peaks in the left panel, four are at periods of 0.998 d, 0.499 d, 0.333 d and 0.153 d, corresponding to the daily sampling and its higher harmonics. The fifth peak at about 24 d yields a non-random but broad distribution of burst phases (Extended Data Fig. 8, bottom left) that most probably reflects non-uniform detections over the 47-d data span. The marginally significant peak at 10.575 ± 0.008 ms in the top-right panel appears to be related to a large multiple of the original 98.304- μ s sample interval of the data. Folding with that period does not show any concentration in pulse phase (Extended Data Fig. 8, bottom right).

In addition to a search for a constant period over the 47-d dataset, we also searched for periods (P) between 1 ms and 1,000 s accompanied by a period derivative (\dot{P}) between 10^{-12} and 10^{-2} ss^{-1} and the same negative \dot{P} range to fold all of the pulses. This also did not reveal any underlying period. In addition, we divided the pulses according to energy with dividing lines at 5×10^{37} erg and 3×10^{38} erg, and found that the pulses in different energy intervals do not have significant periodicity. All observing sessions fall in the predicted active phase of FRB 121102 (refs. ^{44,45}), thus the addition of this sample does not alter the 157-d period found there.

DM variation

Before we can study the detailed emission characteristics of the bursts, the optimum DM should be determined. De-dispersed pulse profiles were created for each DM trial between 500 and 650 pc cm^{-3} with a step size of 0.05 pc cm^{-3} , using the single pulse search tools in Presto³².

Gaussians (multiple when necessary) were fitted to the profiles. The derivative of each Gaussian was then squared. For multiple components, the squared profiles were summed. The optimum DM was then identified according to the maximization of the area under the squared derivative profiles, thus maximizing the structures in the frequency integrated burst profile. The typical DM optimization method and de-dispersed profiles are shown in Extended Data Fig. 9.

The resulting histogram distribution of DMs are shown in Extended Data Fig. 10 (left), the optimal value is $565.8 \pm 0.3 \pm 0.76 \text{ pc cm}^{-3}$, between MJD 58724 and MJD 58776. The two uncertainties are statistical error and systematic error. The latter is estimated by measuring the ΔDM that results in a DM time delay across the whole band equal to half the equivalent width of the bursts (the typical value is 1.5 ms). This suggests that the DM of FRB 121102 has increased by $5\text{--}8 \text{ pc cm}^{-3}$ (1.0–1.4%) with more than 20σ significance compared with earlier detections from MJD 57364; ref.¹⁴ reported the optimal value to be $558.6 \pm 0.3 \pm 1.4 \text{ pc cm}^{-3}$ with similar methodology. Furthermore, the measured DM values and their uncertainties of the bursts are shown in Fig. 4 as a function of individual observations. DM apparently increased over the past 6 years^{15,16} and is found to be consistent with a DM growth rate of $+0.85 \pm 0.10 \text{ pc cm}^{-3} \text{ yr}^{-1}$ in equation (2).

To inspect the reliability of this DM variation trend, we divided the DM measurement into three time bins according to the dates of the event and generated mock DM values in each bin, based on the mean and the standard deviation of the measured DMs in the respective time bins. The null hypothesis was then tested based on the generated DMs under the assumption that DM does not change over time. For each set of generated DM, a slope was fitted. Based on 20,000 trials, the σ of the resulting slope distribution is $0.38 \text{ pc cm}^{-3} \text{ yr}^{-1}$, shown in Extended Data Fig. 10 (right). Thus, the fitted DM growth rate of 0.85 could result from a null hypothesis sample at a 2.6% probability, slightly better than 2σ . This is apparently less significant than the simple fitting, but probably more realistic.

Polarization characteristics

The polarization was calibrated by correcting for differential gains and phases between the receivers through separate measurements of a noise diode injected at an angle of 45° from the linear receivers. The circular polarization of a few brightest bursts is consistent with noise, lower than a few per cent of the total intensity, which agrees with ref.⁶. We searched for the rotation measure (RM) from -6.0×10^5 to $6.0 \times 10^5 \text{ rad m}^{-2}$, a range that is much larger than the $\text{RM} \sim 10^5 \text{ rad m}^{-2}$ reported in ref.⁶, but no significant peak was found in the Faraday spectrum. The linear polarization becomes negligible at L band compared to almost 100% linear polarization at C band reported in ref.⁶. For our data, we estimate the depolarization fraction f_{depol} using

$$f_{\text{depol}} = 1 - \frac{\sin(\Delta\theta)}{\Delta\theta}, \quad (9)$$

where the intra-channel Faraday rotation $\Delta\theta$ is given by

$$\Delta\theta = \frac{2\text{RM}_{\text{obs}}c^2\Delta\nu}{v_c^3}, \quad (10)$$

where c is the speed of light, $\Delta\nu$ is the channel width, and v_c is the central channel observing frequency. Taking $\text{RM}_{\text{obs}} = 10^5 \text{ rad m}^{-2}$ reported in ref.⁶, $\Delta\nu = 0.122 \text{ MHz}$ and $v_c = 1.25 \text{ GHz}$ for our data, we get $f_{\text{depol}} = 20\%$. Although the depolarization fraction is not negligible, the non-detection of the linear polarization cannot be caused by depolarization assuming $\text{RM}_{\text{obs}} < 10^5 \text{ rad m}^{-2}$.

We are confident about the non-detection. We have applied the same analysis procedures to bright pulsars and retrieved expected results. The same procedure has been used in multiple publications^{46–48}. Our non-detection does not conflict with the previous almost 100% linear polarization because all previous polarization detections were

accomplished at frequency bands higher than L band (about 1.4 GHz). Polarization measurements at 4–8 GHz were published in ref.⁶ and at 3–8 GHz in ref.⁴⁹. Unless the RM was somehow much larger during the FAST observations compared to previous determinations, the non-detection appears to require strong frequency evolution of the linear polarization.

Energy budget constraint on the synchrotron maser magnetar model

The total isotropic energy emitted in the 1,652 bursts reported in this paper is $3.4 \times 10^{41} \text{ erg}$. We consider that each FRB has a beaming factor of $f_b = \delta\Omega/4\pi < 1$ (where $\delta\Omega$ is the solid angle of the emission of individual burst). If these individual bursts are isotropically distributed in sky, even though the energy budget for each FRB is smaller by a factor of f_b , there would be also approximately f_b^{-1} more undetected bursts (whose emission beams elsewhere) so that the total energy is not changed²⁷. Adopting a typical radiative efficiency $\eta \sim 10^{-4}\eta_{-4}$ from numerical simulations⁵⁰ (which could be even lower in view of the very rapid repetition rate), the total energy emitted solely during the approximately 60 h of observation spanning 47 d is already $\sim 6.4 \times 10^{46} \eta_{-4}^{-1} \text{ erg}$ (considering FAST only observed about 60 h during these 47 d and assuming that the observed rate applies to the epochs of no observations as well). The total magnetic energy of a magnetar with a surface magnetic field strength $B = 10^{15} B_{15} \text{ G}$ is $\sim (1/6)B^2 R^3 \simeq 1.7 \times 10^{47} \text{ erg}$. The total energy emitted during our observational campaign is already about 37.6% of the available magnetar energy. One possible way to avoid this criticism is to argue that there is a ‘global beaming factor’ $F_b = \Delta\Omega/4\pi$ that is smaller than unity but greater than f_b to describe the beaming angle of all emitted FRBs. This factor could be of the order 0.1 for pulsar-like emission due to the geometry defined by the magnetosphere configuration of the central source. However, for relativistic shocks invoked in the synchrotron maser models, F_b would not be much less than unity due to the lack of a collimation mechanism for a Poynting-flux-dominated outflow.

In view of the fact that FRB 121102 has already been active for nearly a decade and that many faint bursts such as the ones reported in this paper have escaped detection from previous telescopes, we believe that the synchrotron maser model is significantly challenged from the energy budget point of view. A previous analysis using data observed by the Green Bank Telescope⁷ obtained a similar result⁵¹. Even if this global beaming factor $F_b = 0.1$ is assumed, the released energy during this active period is already 3.8% of the total magnetar energy budget. This disfavors the synchrotron maser model and any model that invokes a low radio radiative efficiency.

Data availability

All relevant data for the 1,652 detected burst events are summarized in Supplementary Table 1. Observational data are available from the FAST archive (<http://fast.bao.ac.cn>) 1 year after data collection, following FAST data policy. Owing to the large data volume for these observations, interested users are encouraged to contact the corresponding author to arrange the data transfer. The data that support the findings of this study are openly available in Science Data Bank at <https://doi.org/10.11922/sciencedb.01092> or <https://www.scidb.cn/en/detail?dataSetId=f172ff40142c4100855724b80a085deb>.

Code availability

Computational programs for the FRB121102 burst analysis and observations reported here are available at <https://github.com/NAOC-pulsar/PeiWang-code>. Other standard data reduction packages are available at their respective websites: PRESTO (<https://github.com/scottransom/presto>), HEIMDALL (<http://sourceforge.net/projects/heimdall-astro/>), DSPSR (<http://dspsr.sourceforge.net>), PSRCHIVE (<http://psrchive.sourceforge.net>).

31. Petroff, E. et al. A real-time fast radio burst: polarization detection and multiwavelength follow-up. *Mon. Not. R. Astron. Soc.* **447**, 246 (2015).
32. Ransom, S. M. *New Search Techniques for Binary Pulsars*. PhD thesis, Harvard Univ. (2001).
33. Zhang, B. Fast radio burst energetics and detectability from high redshifts. *Astrophys. J. Lett.* **867**, L21 (2018).
34. Gupta, V. et al. Estimating fast transient detection pipeline efficiencies at UTMOST via real-time injection of mock FRBs. *Mon. Not. R. Astron. Soc.* **501**, 2316–2326 (2021).
35. Luo, R., Lee, K., Lorimer, D. R. & Zhang, B. On the normalized FRB luminosity function. *Mon. Not. R. Astron. Soc.* **481**, 2320–2337 (2018).
36. Wang, F. Y. & Zhang, G. Q. A. Universal energy distribution for FRB 121102. *Astrophys. J.* **882**, 108 (2019).
37. Lu, W. & Piro Anthony, L., Implications from ASKAP fast radio burst statistics. *Astrophys. J.* **883**, 3796–3847 (2019).
38. Luo, R. et al. On the FRB luminosity function—II. Event rate density. *Mon. Not. R. Astron. Soc.* **494**, 665–679 (2020).
39. Cordes, J. M., Bhat, N. D. E., Hankins, T. H., McLaughlin, M. A. & Kern, J. The brightest pulses in the universe: multifrequency observations of the Crab pulsar's giant pulses. *Astrophys. J.* **612**, 375–388 (2004).
40. The CHIME/FRB Collaboration et al. CHIME/FRB detection of eight new repeating fast radio burst sources. Preprint at <https://arxiv.org/abs/1908.03507> (2019).
41. Oppermann, N., Yu, H. R. & Pen, U. L. On the non-Poissonian repetition pattern of FRB121102. *Mon. Not. R. Astron. Soc.* **475**, 5109–5115 (2018).
42. Lomb, N. R. Least-squares frequency analysis of unequally spaced data. *Astrophys. Space Sci.* **39**, 447–462 (1976).
43. Scargle, J. D. Studies in astronomical time series analysis. II. Statistical aspects of spectral analysis of unevenly spaced data. *Astrophys. J.* **263**, 835–853 (1982).
44. Rajwade, K. M. et al. Possible periodic activity in the repeating FRB 121102. *Mon. Not. R. Astron. Soc.* **495**, 3551–3558 (2020).
45. Cruces, M. et al. Repeating behaviour of FRB 121102: periodicity, waiting times and energy distribution. Preprint at <https://arxiv.org/abs/2008.03461> (2020).
46. Feng, Y. I. et al. Study of PSR J1022+1001 using the FAST radio telescope. *Astrophys. J.* **908**, 105–111 (2021).
47. Luo, R. et al. Diverse polarization angle swings from a repeating fast radio burst source. *Nature* **586**, 693–696 (2020).
48. Zhang, C. F. et al. A highly polarised radio burst detected from SGR 1935+2154 by FAST *The Astronomer's Telegram* **13699**, 1–1 (2020).
49. Hilmarsson, G. H., et al, Rotation measure evolution of the repeating fast radio burst source FRB 121102 *Astrophys. J. Lett.* **908**, 10–23 (2021).
50. Plotnikov, I. & Sironi, L. The synchrotron maser emission from relativistic shocks in fast radio bursts: 1D PIC simulations of cold pair plasmas. *Mon. Not. R. Astron. Soc.* **485**, 3816–3833 (2019).
51. Wu, Q., Zhang, G. Q., Wang, F. Y. & Dai, Z. G. Understanding FRB 200428 in the synchrotron maser shock model: consistency and possible challenge. *Astrophys. J. Lett.* **900**, L26 (2020).

Acknowledgements This work is supported by National Natural Science Foundation of China (NSFC) programme nos. 11988101, 11725313, 11690024, 12041303, U1731238, U2031117, U1831131 and U1831207; by CAS International Partnership programme no. 114-A11KYSB20160008; by CAS Strategic Priority Research programme no. XDB23000000; the National Key R&D Program of China (no. 2017YFA0402600); and the National SKA Program of China no. 2020SKA0120200; and the Cultivation Project for FAST Scientific Payoff and Research Achievement of CAMS-CAS. S.C. and J.M.C. acknowledge support from the U.S. National Science Foundation (AAG 1815242). D.R.L. acknowledges support from the U.S. National Science Foundation awards AAG-1616042, OIA-1458952 and PHY-1430284. P.W. acknowledges support from the Youth Innovation Promotion Association CAS (ID 2021055) and CAS Project for Young Scientists in Basic Research (grant YSBR-006); P.W. and C.H.N. acknowledge support from cultivation project for FAST scientific payoff and research achievement of CAMS-CAS. Q.J.Z. is supported by the Technology Fund of Guizhou Province ((2016)-4008). L.Q. is supported by the Youth Innovation Promotion Association of CAS (ID 2018075). This work made use of data from FAST, a Chinese national mega-science facility built and operated by the National Astronomical Observatories, Chinese Academy of Sciences.

Author contributions D.L., R.D. and W.W.Z. launched the FAST campaign; P.W., C.H.N., Y.K.Z., Y.F., N.Y.T., J.R.N., C.C.M. and L.Z. processed the data; D.L., B.Z. and P.W. drafted the paper; R.D., X.X.Z., V.G., C.J., Y.Z., D.W. and Y.L.Y. built the FAST FRB backend; L.Q., G.H., X.Y.X., Q.J.Z. and S.D. made key contributions to the overall FAST data processing pipelines; L.S., M.C. and M.K. provided salient information on FRB 121102 from other observatories, particularly Effelsberg, and contributed to the scientific analysis; S.C., J.M.C., D.R.L. and F.Y.W. contributed to the writing and analysis, including simulations of the waiting time distribution (J.M.C.). F.Y.W. and G.Q.Z. contributed to work on the time-dependence of bimodal energy distribution.

Competing interests The authors declare no competing interests.

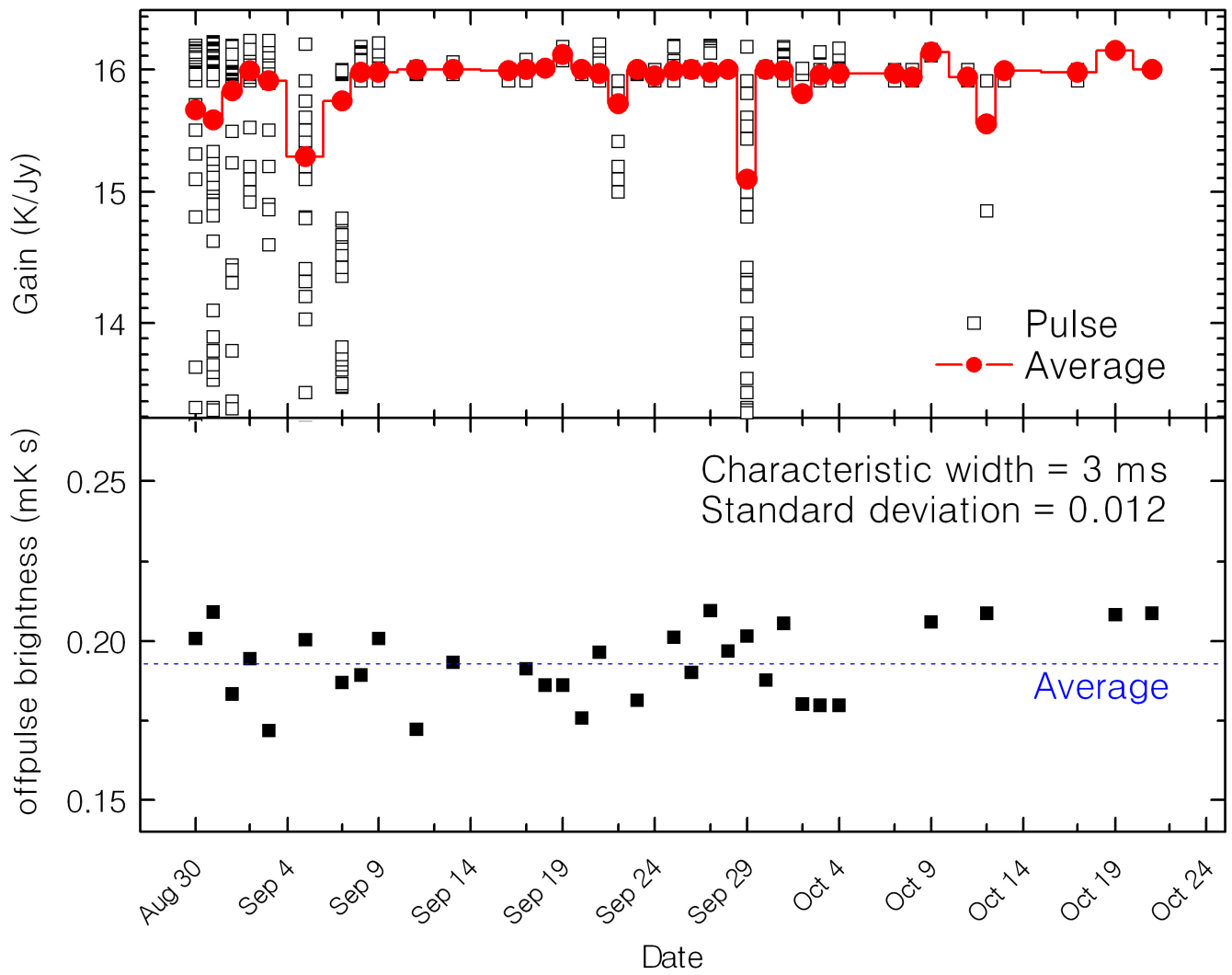
Additional information

Supplementary information The online version contains supplementary material available at <https://doi.org/10.1038/s41586-021-03878-5>.

Correspondence and requests for materials should be addressed to D. Li or B. Zhang.

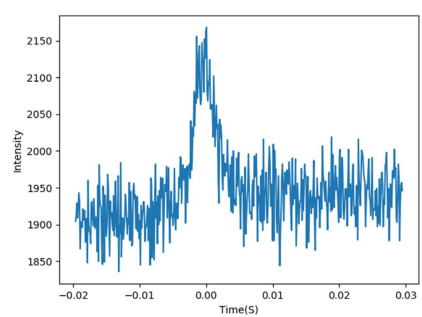
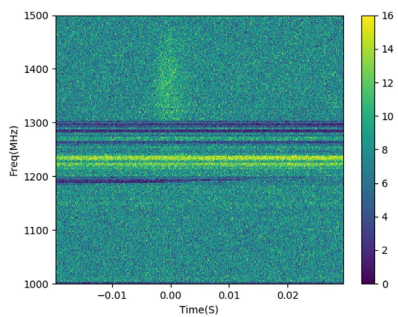
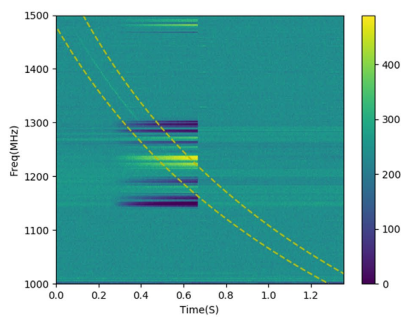
Peer review information *Nature* thanks Victoria Kaspi and the other, anonymous, reviewer(s) for their contribution to the peer review of this work. Peer reviewer reports are available.

Reprints and permissions information is available at <http://www.nature.com/reprints>.



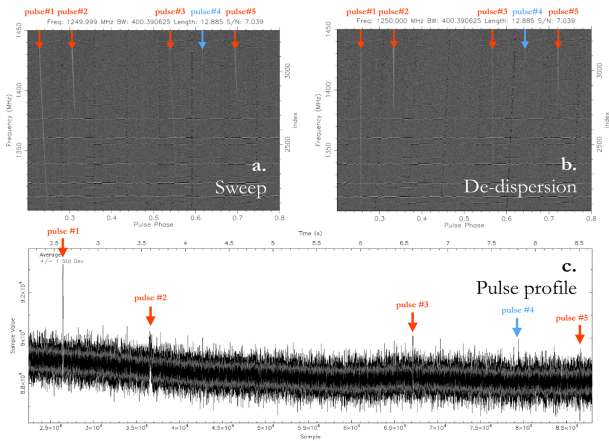
Extended Data Fig. 1 | The distribution of the instrumental gain and off-pulse brightness RMS at 1.25 GHz for observations. The upper panel indicates the gain applied for each pulses. The red dots denote the averaged

gain in each day. The bottom panel shows the off-pulse brightness RMS (mK s) of the first pulse detected each day.

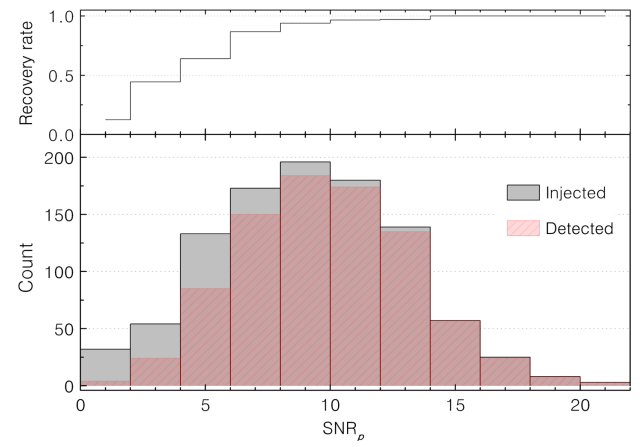


Extended Data Fig. 2 | Example of a dynamic spectrum of burst with RFI.

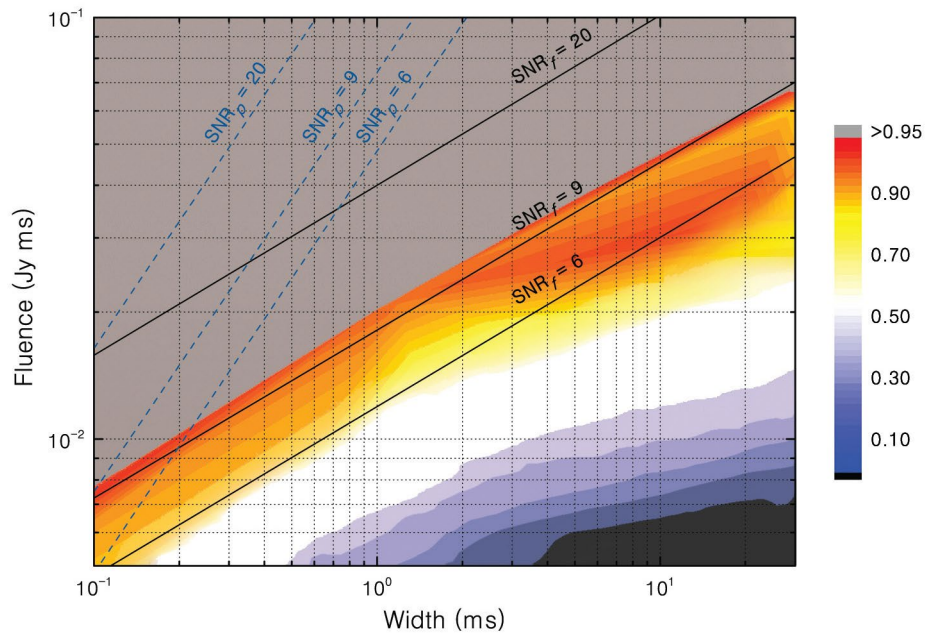
Article



Extended Data Fig. 3 | Left panel: Example of FRB simulations. Upper panels (a and b) are injected and de-dispersed dynamic spectra respectively. The time series is shown in panel (c) with the red arrows pointing to simulated pulses that were detected, while the blue arrow indicates an undetected pulse.

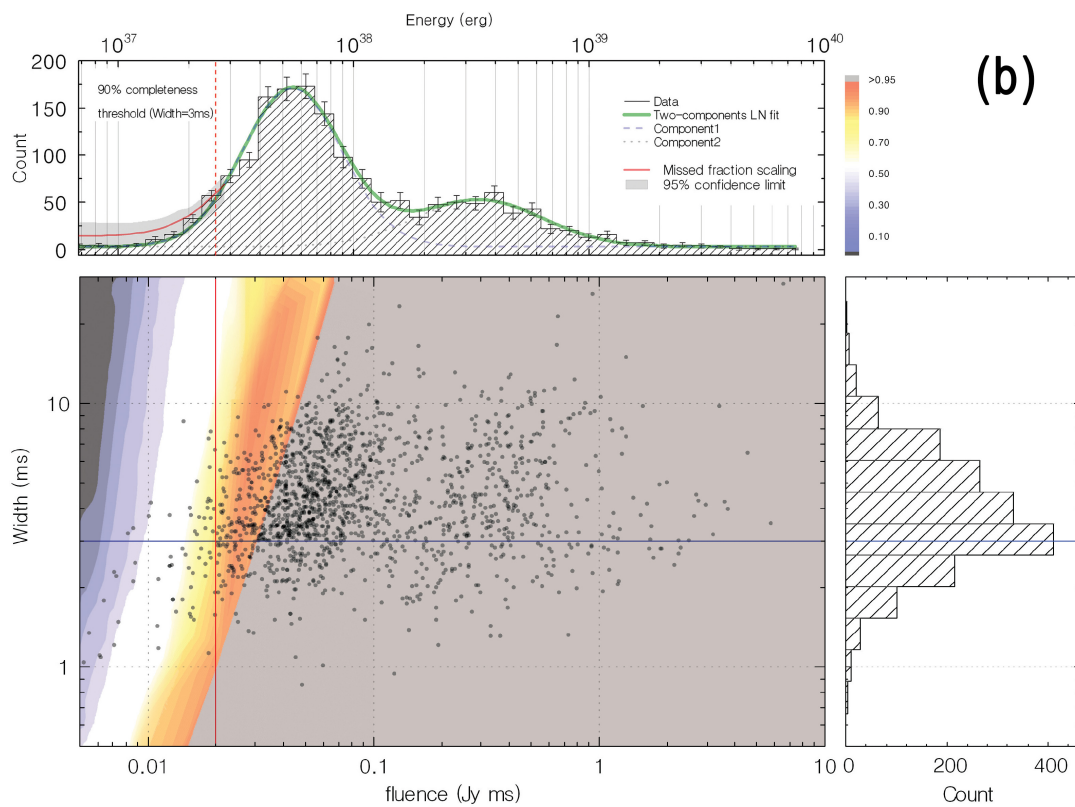
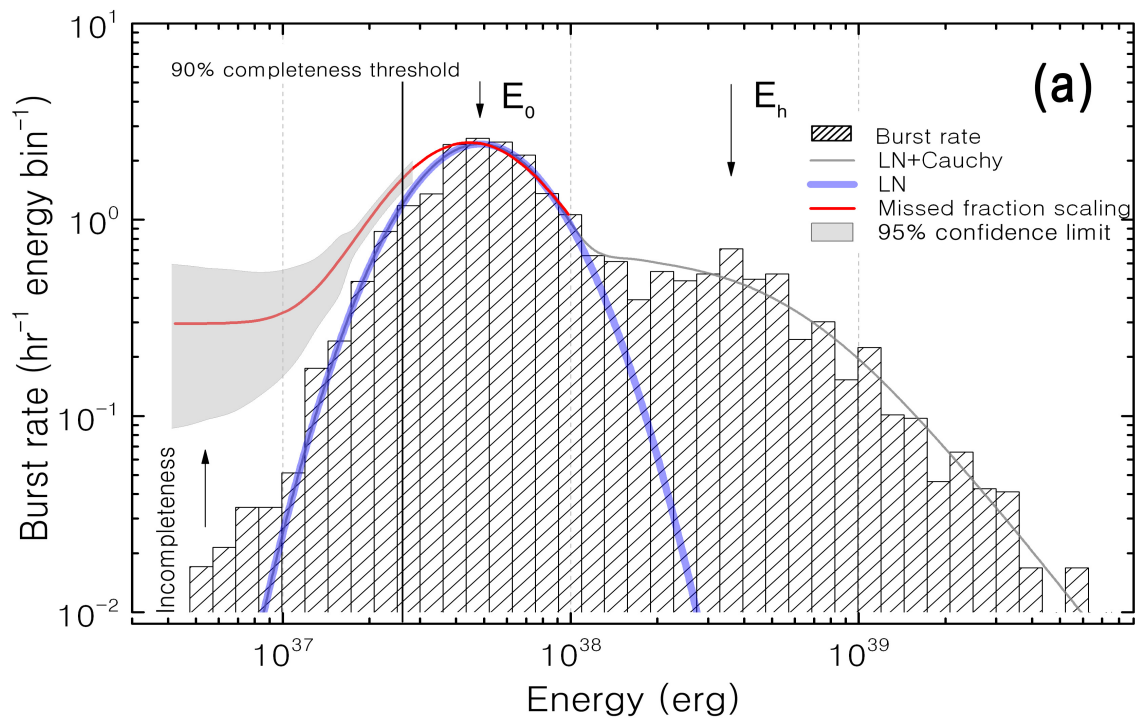


Right panel: Comparison of SNR_p recovered by FRB search versus the corresponding injected values. The SNR_p histograms separately indicate the injected FRB pulses (grey lines) and the mock FRBs detected (red lines).



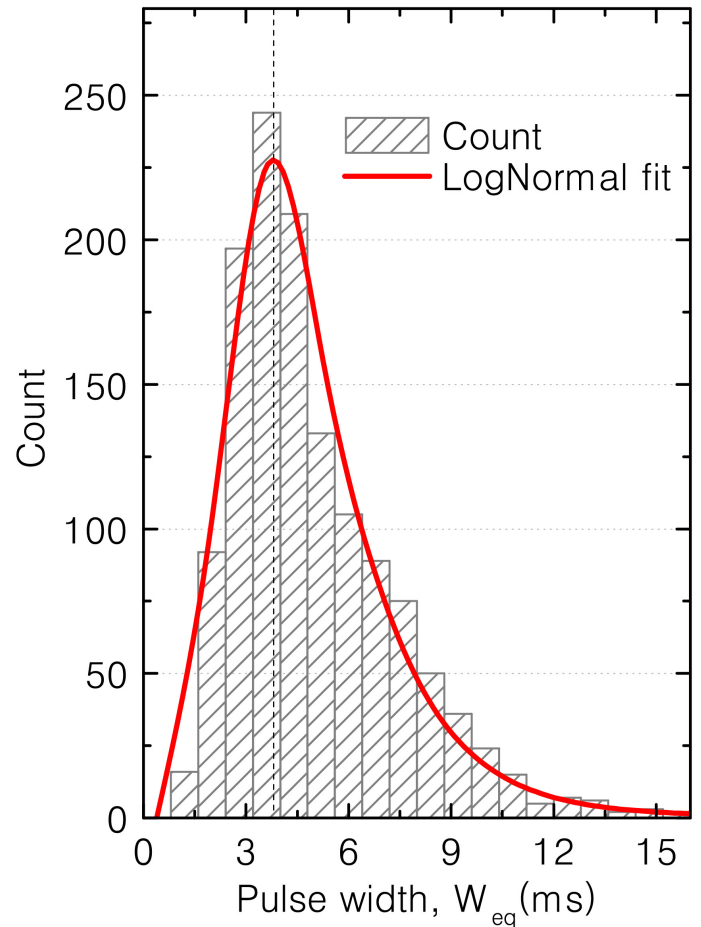
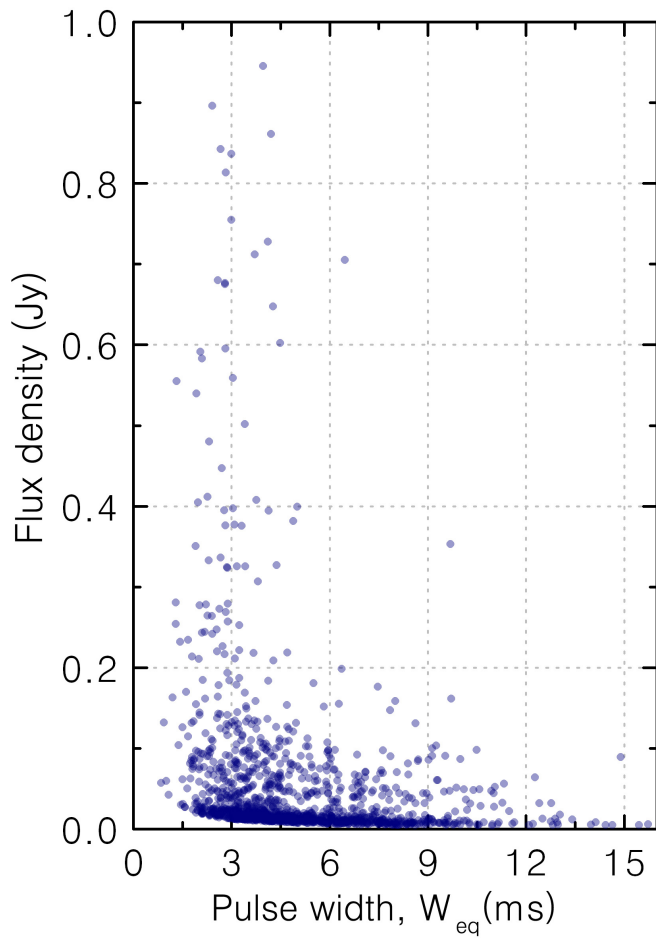
Extended Data Fig. 4 | The completeness fraction of the FAST survey to FRBs as a function of the observed fluence and detected width. All FRBs lying in the integrated SNR_f < 6 region are below PRESTO’s search threshold. The region above the integrated SNR_f of 6 shows the incompleteness of our FAST detection to broad FRBs as revealed by the injections. The map was

smoothed (rebin) the map with a box of 0.05 ms × 0.002 Jy ms, which ensured the presence of at least one injected pulse in most map areas. Then for a few grid points without pulses, a simple linear interpolation was used to improve the visual appearance. The colour bar on the right side indicates the detection recovery fraction.

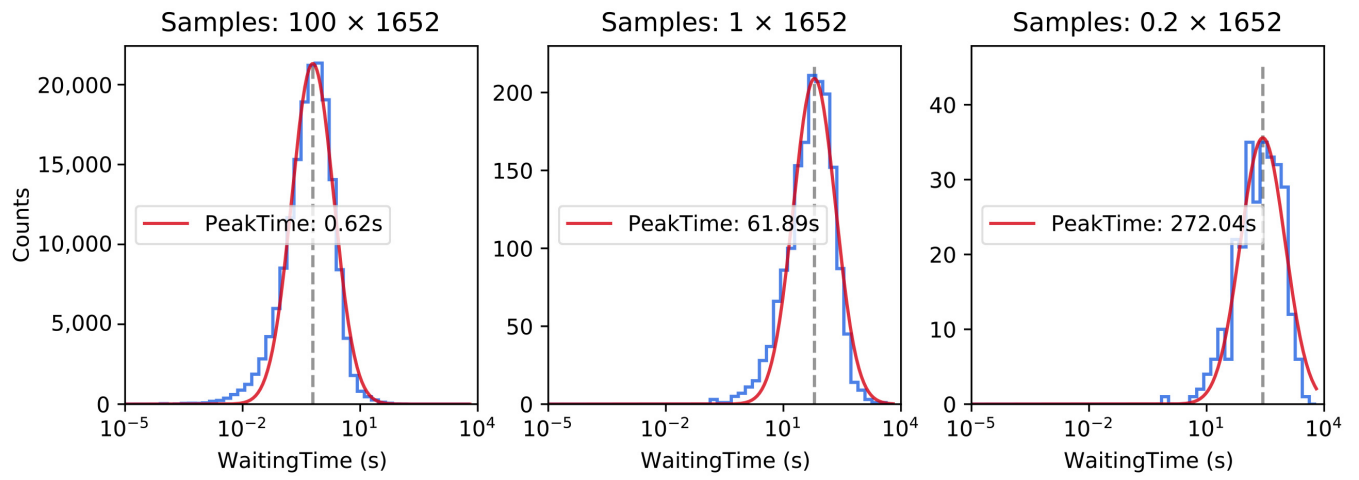


Extended Data Fig. 5 | Upper panel (a): The burst rate distribution of the isotropic equivalent energy. Details as per Extended Data Fig. 2. The red line represents the recovered distribution by adding back the missing fraction based on the simulation. The grey shaded region is the uncertainty for a 95% confidence based on the Poisson statistical assumption in the “reconstructed” fitting. **Bottom panel (b): The fluence-width distribution at 1.25 GHz for**

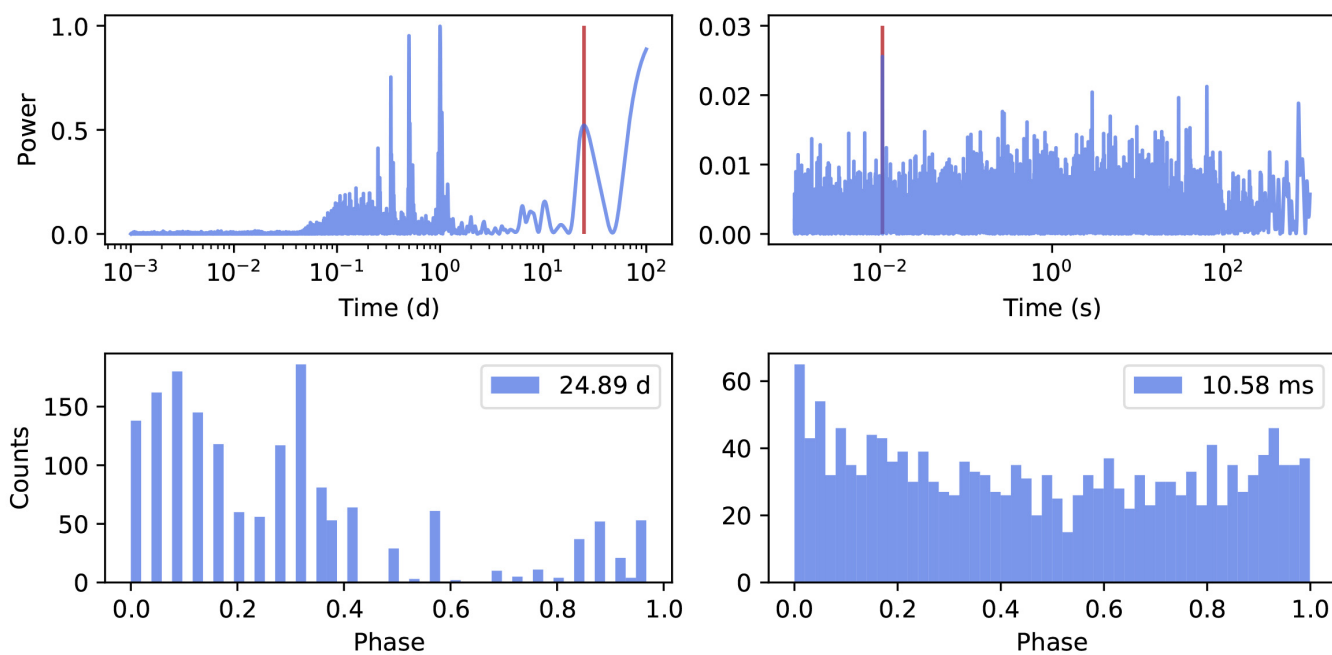
FRB 121102 bursts. The black dots indicate the 1,652 detected bursts, the colorbar is consistent with Extended Data Fig. 4. In the upper panel, the two-component lognormal (LN) distribution is separately fitted in blue dashed line and grey dot line, an overall fit for bursts is shown in green. The red line and the shaded region indicates reconstructed missing fraction of bursts detection and uncertainty.



Extended Data Fig. 6 | Flux intensity and pulse width distribution of FRB 121102. *Left:* Flux intensity against pulse width for the FRB 121102 bursts with peak $\text{SNR}_p > 10$ in our sample. *Right:* The equivalent pulse width histogram.

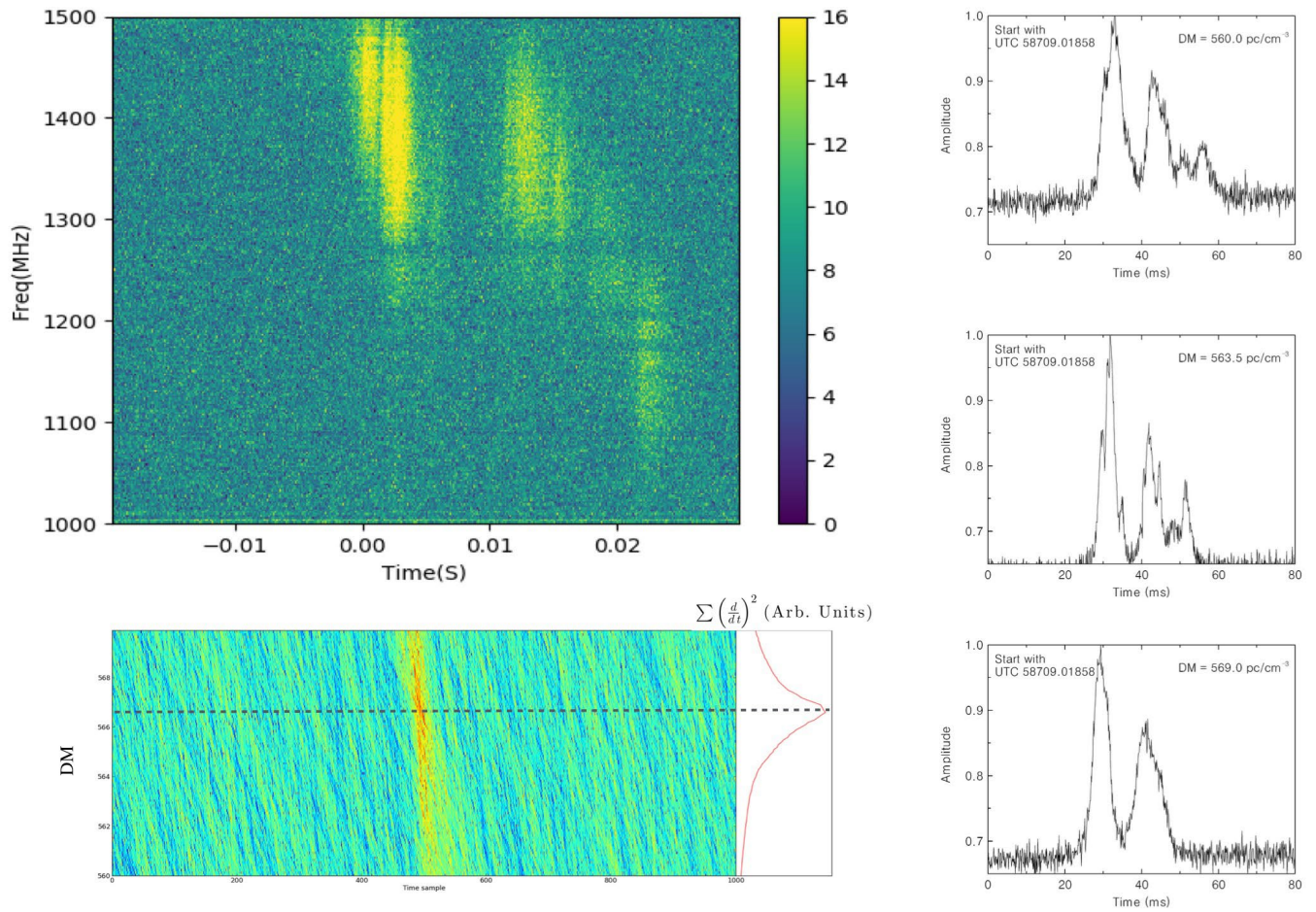


Extended Data Fig. 7 | MC simulations of the waiting time distribution. The three figures correspond to three different simulations, and the number of randomly generated pulses in each simulation are $100 \times 1652 - 1.6e5$, $1 \times 1652 = 1652$, and $0.2 \times 1652 - 330$. The peak times of the three log-normal distributions are 0.62 s, 61.89 s, and 272.04 s, respectively.

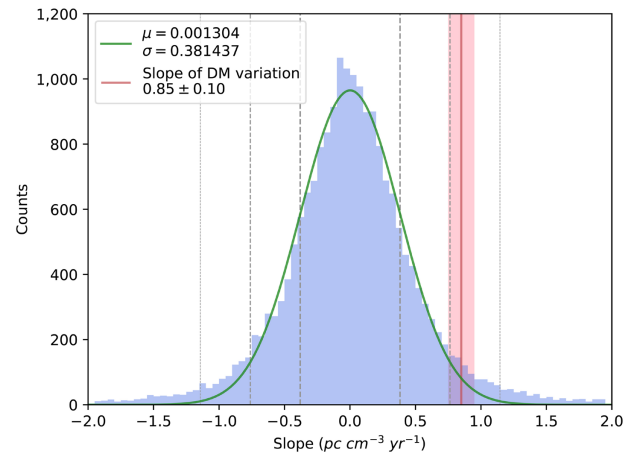
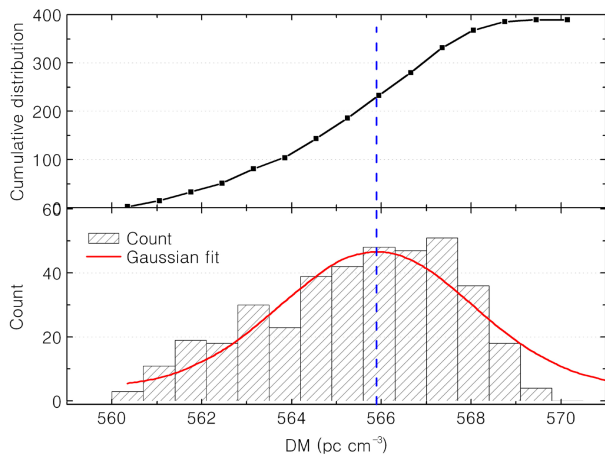


Extended Data Fig. 8 | Lomb-Scargle periodograms of FRB 121102 burst arrival times (top row) along with phase histograms for two trial periods (bottom row). Left: Periods from 10^{-3} to 10^2 d. The four leftmost peaks in the periodogram are caused by daily sampling and its harmonics. The peak at ~24 d

is related to the sampling window function (i.e. non-uniform sampling) over the 47 d data set, as is consistent with the broad distribution in burst phase (bottom left). Right: Periods from 1 ms to 10^3 s. The peak at 10 ms is a large multiple of the original sampling time and also yields no distinct concentration in burst phase.



Extended Data Fig. 9 | Example of the DM optimization method for FRB 121102. The complex time–frequency structures for the burst of MJD 58729.01858 was revealed with an optimal DM of 563.5 pc cm^{-3} .



Extended Data Fig. 10 | Left panel: Histogram and cumulative distribution of dispersion measure for FRB 121102. Right panel: Slope distribution of null hypothesis test.